# Stability and Compressibility of Cation-doped High-Entropy Oxide $MgCoNiCuZnO_5$

Jian Chen[1,2] ，Weixin Liu[2], Junxiu Liu[2] ，Xiaoliang Zhang[2], Mingzhi Yuan[2] ，Yunlei Zhao[2], Jiejuan Yan[2,3] ，Mingqiang Hou[2,3] ，Jinyuan Yan[3], Martin Kunz[3], Nobumichi Tamura[3], Hengzhong Zhang[2,*] , Zhoulan Yin[1,*]

*1.School of Chemistry and Chemical Engineering, Central South University, Changsha, Hunan 410083, China.*

*2. Center for High Pressure Science and Technology Advanced Research, Shanghai 201203, China.*

*3. Advanced Light Source, Lawrence Berkeley National Laboratory, Berkeley, CA 94720, United States*

**ABSTRACT:** High-entropy oxides (HEOx) are multicomponent (≥5) complex oxides that possess material properties and functions unexpected from their constituent simple oxides. Previous studies demonstrated that a cation-doped HEOx, $MgCoNiCuZnO_5$, shows good catalytic activity, excellent ionic conductivity and high capacity in energy storage. The structural and mechanical stabilities of materials are pivotal to their applications. However, how temperature and pressure influence the structural stability of cation-doped HEOx and how doping affects the mechanical properties are yet to be understood. In this work, we investigated the structural stabilities of undoped and Li/Mn-doped $MgCoNiCuZnO_5$ in heating or under compression using in-situ synchrotron X-ray diffraction (XRD), and determined their elastic moduli using high-pressure XRD. Our results show that the HEOx compounds are structurally stable at temperatures up to ~ 450 °C or at pressures up to ~ 50 GPa, and that Li/Mn doping makes the HEOx more compressible. Our molecular static (MS) calculations predicted that the formation reaction of a HEOx is endothermic, consistent with the fact that a single-phase HEOx can only be produced at high temperatures. The MS calculations also revealed that the observed doping-induced elastic softening stems from the introduction of the Li-O/Mn-O ionic bonds to the HEOx compound, which are weaker than

other cation-oxygen ionic bonds in the undoped HEOx. These findings will be indispensable to engineering the HEOx materials for use in ion batteries, catalysis and other fields.

# 1. INTRODUCTION

High-entropy oxides (HEOx) are a new class of multi-component (usually $\geq 5$) complex oxides that possess material properties different from the simple combination of those of their constituent simple oxides. The first HEOx, $MgCoNiCuZnO_5$, was synthesized through high-temperature solid-state reactions in 2015.[1] Later studies show that $MgCoNiCuZnO_5$ can generate high capacity in lithium battery energy storage;[2] Pt-doped $MgCoNiCuZnO_5$ can produce stable and efficient catalytic oxidation of carbon monoxide;[3] Li/Na-doped $MgCoNiCuZnO_5$ has very high ionic mobility and electrical conductivity,[4] and a similar compound $(FeMgCoNi)O_{1.2}$ exhibits high efficiency in thermochemical water splitting.[5] Recently, other kinds of HEOx compounds with different chemical compositions and in perovskites structures,[6-7] fluorite structures[8-10] and spinel structures[11] have been synthesized. With these diversities in the structures and chemical compositions, HEOx compounds are promising in contributing to clean and renewable energy.

The structural stability of HEOx as a function of temperature (T) and pressure (P) is critical to their applications. For instance, in Li-doped HEOx ion batteries, accompanying charging and discharging,

the system enthalpy and volume change repeatedly, which can cause temperature and pressure fluctuations in the cell, making the battery system unstable and even malfunction. Thus, it is necessary to optimize the cell design and fabrication of the whole battery system with knowledge of the stability and mechanical properties of the HEOx materials. However, a comprehensive understanding of how T&P affect the stability of HEOx is lacking so far. How doping affects the mechanical properties of HEOx is also unknown. Thus, in this work, we developed different routes to synthesize Li- and Mn-doped $MgCoNiCuZnO_5$, considering that Mn-doping can enhance the stability and performance of lithium ion battery materials.[12] Then, using in-situ synchrotron X-ray diffraction (XRD), we studied their thermal stability while in heating and mechanical stability while under compression. These experiments enable us to identify the effects of doping, temperature and pressure on the structures and mechanical properties of undoped and Li/Mn-doped $MgCoNiCuZnO_5$. Further, molecular simulations were used to probe the intrinsic mechanism accounting for the observed structure-property relationship. The findings from this work will provide essential knowledge for developing novel applications of the new materials.

## 2. EXPERIMENTAL SECTION

**2.1. Chemicals.** Magnesium oxide (MgO, 99.9% wt.), cobalt oxide (CoO, AR), nickel oxide (NiO, 99.5% wt.), cupric oxide (CuO, 99.5% wt.) and zinc oxide (ZnO, 99.9% wt.) were purchased from Macklin Biochem. Co. Ltd (Shanghai). Manganese monoxide (MnO, 99% wt.) and lithium carbonate ($Li_2CO_3$, 99.9% wt.) were purchased from Aladdin Bio-Chem. Tech. Co., Ltd.(Shanghai). All chemicals were used directly without further purification.

**2.2. Sample preparations**

**2.2.1. Preparation of undoped $MgCoNiCuZnO_5$ (u-HEOx).** Following ref. 1, undoped $MgCoNiCuZnO_5$ (that can also be written as (Mg,Co,Ni,Cu,Zn)O or $(Mg_{0.2}Co_{0.2}Ni_{0.2}Cu_{0.2}Zn_{0.2})O$ and denoted as u-HEOx hereafter) was synthesized using solid-state reaction at high temperature. Powders of equimolar MgO, CoO, NiO, CuO and ZnO were mixed well in an agate mortar and then ground for 6 hours for attaining uniform dispersions of the constituent oxides among each other. The well mixed powders were then cold-compressed into a thin disk ~ 10 mm in diameter and ~ 1 mm in thickness under a pressure of ~ 300 MPa**.** The disk was then heated at 1100 °C in air for 3 hours in a tube furnace, followed by quenching to room temperature in air.

**2.2.2. Preparation of Li-doped $MgCoNiCuZnO_5$(Li-HEOx).** Bérardan et al. doped $Li^+$ in $MgCoNiCuZnO_5$ using $Li_2CO_3$ as the lithium source via solid-state reaction at 1000 °C.[13] When synthesizing Li-doped HEOx at such a high temperature using this one-step route, Li in the raw mixture may volatilize due to the low melting point of $Li_2CO_3$ (~ 723°C)[14]. This might cause deviation of the lithium content from the desired stoichiometry. Therefore, in this work, we proposed a two-step synthesis route, attempting to reduce the lithium loss. First, a powder mixture with a molar ratio of MgO:CoO:NiO:CuO:ZnO:$Li_2CO_3$ =1:1:1:1:1:0.13 was prepared，which would produce a Li-doped HEOx with a nominal formula of $(Mg,Co,Ni,Cu,Zn)_{0.95}Li_{0.05}O_{0.975}$ if there is no Li loss. The mixture was cold-compressed and heated at 720 °C in air for 6 hours in order to introduce partial reaction of $Li_2O$ with other oxide components, which was formed from gradual decomposition of $Li_2CO_3$ around its melting point. Then, the sample was heated at 1100 °C in air for 3 hours, followed by quenching to room temperature in air.

**2.2.3. Preparation of Mn-doped $MgCoNiCuZnO_5$ (Mn-HEOx).** In previous work,[15] ions of Sc, Cr, Sb, Ge and Sn have been successfully doped in $MgCoNiCuZnO_5$ while maintaining a stable rocksalt structure. Doping of Mn in HEOx has not been reported so far. In this work, we used following method to dope Mn in $MgCoNiCuZnO_5$. A powder mixture

of MgO, CoO, NiO, CuO, ZnO and MnO in the molar ratio of 1:1:1:1:1:0.26 was ground and cold-compressed to form disks, as described above. Then, three of the disks were heat-treated in air for 3 hours at 1100, 1300 and 1500 °C, respectively, followed by quenching to room temperature in air. The prepared samples would have a nominal formula of $(Mg,Co,Ni,Cu,Zn)_{0.95}Mn_{0.05}O$.

**2.3. Characterization of sample structures and elemental distributions.** XRD patterns of synthesized samples were collected using a PANalytical Empyrean X-ray diffractometer operated at 40 kV and 40 mA, with a Cu $K_\alpha$ radiation (X-ray wavelength 1.5406 Å). Scanning electron microscopy (SEM) image of the samples were taken using a FEI Versa 3D dual-beam FIB/SEM operated at 25 kV. Elemental mapping of the samples was carried out using the energy-dispersive X-ray spectroscopy (EDXS) of the SEM. All samples were characterized by XRD for phase identifications, by SEM for morphology examinations, and by EDXS for elemental mapping.[6, 8, 16] Lattice parameters of the samples at room-temperature were determined accurately from XRD data of the samples with Si as an internal $2\theta$ calibrant. Transmission electron microscope (TEM) examinations of the samples were conducted using a JEOL 2100 TEM instrument with a general double tilt sample holder. As the samples were sensitive to electron beam

irradiation, TEM images were taken using a middle beam spot size (no.3) and at a small current density of 19.2 μA $cm^{-2}$. These operating parameters were helpful in controlling the radiation damage of the samples. Selected area electron diffraction (SAED) patterns were collected with a SAED aperture of 15 μm.

**2.4. Determination of lithium contents in Li-doped HEOx samples.** Due to possible volatilization of lithium at high temperature, the actual Li content of a Li-doped sample may deviate from the prepared value. Thus, the Li contents of Li-HEOx samples prepared from the one-step and two-step routes were determined using inductively coupled plasma-atomic emission spectrometry (ICP-AES; Optima 5300DV). A sample of ~ 0.1 g was dissolved in a glass beaker using a hydrochloric acid while in heating on a stove, and then transferred to a measuring flask. The solution was diluted using a 1 % nitric acid to form a 50 mL solution. This solution was then used to do the ICP-AES measurement of the Li concentration at an optimal AES wavelength of 670.784 nm. The needed calibration curve was generated from Li standard solutions containing 1, 5 and 10 ppm Li. The precision of the determined Li concentration is ~ 95 %.

**2.5. *In-situ* high-temperature X-ray diffraction.** *In-situ* high-temperature (HT) XRD was conducted at the micro-XRD beamline

station 12.3.2 of the Advanced Light Source (ALS) at the Lawrence Berkeley National Laboratory. All HEOx samples were ground to fine powders and then pressed into thin disks ~ 5 mm in diameter and ~ 1 mm in thickness. The disks were glued to the heating surface of an Anton Paar DHS 900 heating stage mounted on the sample stage of the beamline station. Before heating, ambient XRD patterns of samples were collected at room temperature and in air. In-situ heating XRD experiments were conducted in a flowing nitrogen gas while the heating stage was enclosed by a graphite dome lid. This kept thermal stability of the samples and prevented direct thermal irradiation to the X-ray detector. The samples were heated from room temperature to ~ 450°C at a step of 50 °C and with a stay time of ~ 0.5 h at each temperature.

A focused monochromatic X-ray beam (energy 10 keV) ~10 μm in diameter was used to scan a chosen sample area of ~ 200×200 $\mu m^2$. The diffracted X-ray beams were recorded using a DECTRIS Pilatus 1M hybrid pixel array detector. The sample-to-detector distance was calibrated using an $Al_2O_3$ standard powder sample. The collected diffraction images were processed using the software XMAS,[17] yielding numerical intensity *vs* diffraction angle data. The XRD patterns from the whole scanning area were averaged to yield an average XRD

pattern of the sample at a given temperature.

**2.6. *In-situ* high-pressure X-ray diffraction.** *In-situ* high-pressure (HP) XRD experiments were performed at the high-pressure beamline 12.2.2 of ALS.[18] The pressure on a sample was generated using a diamond anvil cell (DAC) with an anvil culet size of ~ 300 μm. A T301 stainless steel gasket with a thickness of ~ 250 μm was pre-indented to ~ 30 μm in thickness and then drilled through its center using laser ablation, forming a hole of ~ 120 μm in diameter to serve as the sample chamber. A small amount of fine sample powders was loaded into the sample chamber together with 1 – 3 small ruby balls as the pressure calibrant for measuring pressure using the fluorescence method. Neon or a methanol-ethanol mixture (volume ratio of 4:1) was used as the pressure transmitting medium. The DAC loaded with the sample was then mounted to the sample stage of the beamline station for HP-XRD.

HP-XRD patterns were collected at a beam energy of 25 keV (wavelength 0.4959 Å) with a beam size of ~ 15 μm. A MAR345 image plate was used to record the diffraction images, which were then converted to the numerical intensity *vs* $2\theta$ data using the Fit2d or Dioptas program.[19] The sample-to-detector distance was calibrated using a $CeO_2$ standard sample. The lattice parameters of the HEOx

samples at different pressures were derived from Rietveld fitting of the XRD patterns using the GSAS + EXPGUI software.[20]

## 3. COMPUTATIONAL SECTION

In order to explore the mechanism underlying the doping effect on the elasticity of HEOx, we used molecular static (MS) calculations to calculate the bulk moduli of u-HEOx, Li-HOEx, Mn-HEOx, as well as their constituent simple oxides. In the calculations, the interaction potential ($u_{ij}$) between atoms i and j was described by the Buckingham potential function

$$u_{ij}=\frac{Z_i Z_j}{r_{ij}}+A_{ij}\exp\left(\frac{-r_{ij}}{\rho_{ij}}\right)-\frac{C_{ij}}{r_{ij}^6} \qquad (1)$$

The first term on the right-hand side (rhs) of equation 1 represents the electrostatic interaction between atoms i & j, and the rest of the rhs represents the short-range (repulsive and van der Waals) interaction between them. In above equation, $z_i$ and $z_j$ are, respectively, the electric charges of atoms i & j, $r_{ij}$ is the distance between them, and $A_{ij}$, $r_{ij}$ and $c_{ij}$ are potential function parameters pertinent to the atomic pair i & j.

In our MS calculations, the cations concerned include $Mg^{2+}$, $Co^{2+}$,

$Ni^{2+}$, $Cu^{2+}$, $Zn^{2+}$, $Mn^{2+}$ and $Li^{+}$, and the only anion is $O^{2-}$. Following previous work,[21] all cations are modeled as simple point charges, while the oxygen anion $O^{2-}$ is modeled using the shell model.[22] That is, O atom is treated as a core and a massless (or very light) shell that is connected by a spring, accounting for the ionic polarization induced under a local electric field. The potential function parameters for the atomic pairs Co-O, Ni-O, Zn-O and O-O were taken from those derived by Lewis et al. (Table 1 of ref. 21), as compiled in the force field library of the General Utility Lattice Program (GULP)[23]. For the atomic pairs Mg-O, Cu-O, Mn-O and Li-O, we derived the potential function parameters using empirical fitting to available material properties using the program GULP (v.5.1)[23] (see Table S1 in Supporting Information (SI)). The program GULP was again used to conduct the MS calculations. First, the crystal structure of a concerned oxide (including MgO, CoO, NiO, CuO, ZnO, MnO, $Li_2O$, u-HEOx, Li-HEOx and Mn-HEOx) was optimized. Then, the bulk modulus and the lattice energy (adopting definition in ref. 14) of the compound were computed.

## 4. RESULTS AND DISCUSSION

### 4.1. Characterization of undoped $MgCoNiCuZnO_5$ (u-HEOx).

XRD, SEM/ EDXS and TEM/SAED were used to characterize the synthesized sample (Figure 1). The XRD pattern of u-HEOx in Figure 1a shows that the synthesized sample is crystalline and in a rocksalt structure, consistent with a previous work.[1] Rietveld fitting [24] of the XRD pattern (with an internal standard Si; Figure 2) using the periclase phase of MgO (space group $Fm\acute{3}m$) as the structure model gave a lattice parameter of $a$ = 4.238 ± 0.003 Å. The SEM image (Figure 1b) shows that the sample contains lots of grains with sizes varying from sub-microns to ~ 25 μm, with a typical grain size of ~ 10 μm. EDXS elemental mapping of the sample (Figure 1c, and Figures S1 & S2 in SI at a relatively high resolution) shows that the constituent elements are uniformly distributed in the sample, and hence no phase segregations are present. The SAED pattern (Figure 1d) shows that the very fine particles produced by grinding are still crystalline. Since the sample is crystalline from very fine sizes (Figure 1d) to bulk sizes (Figure 1a), the SEM image in Figure 1b unveils the polycrystalline nature of the synthesized sample.

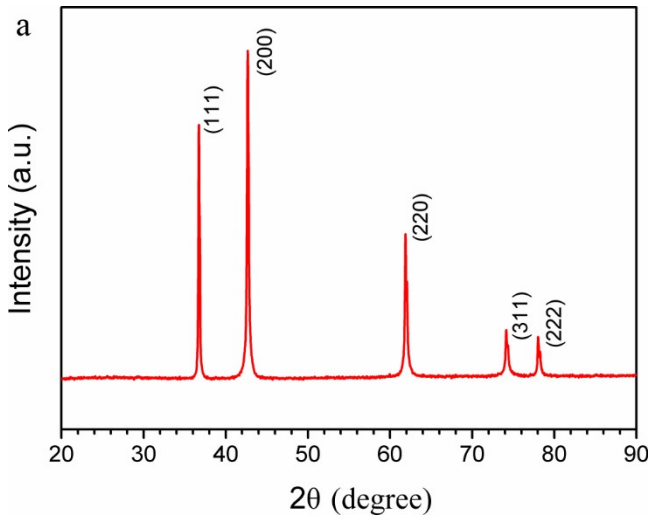
a
Intensity (a.u.)
(111)
(200)
(220)
(311)
(222)
20
30
40
50
60
70
80
90
2θ (degree)

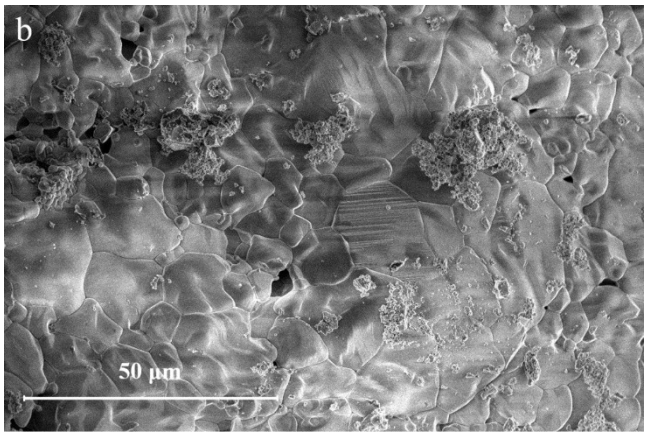
b
50 µm

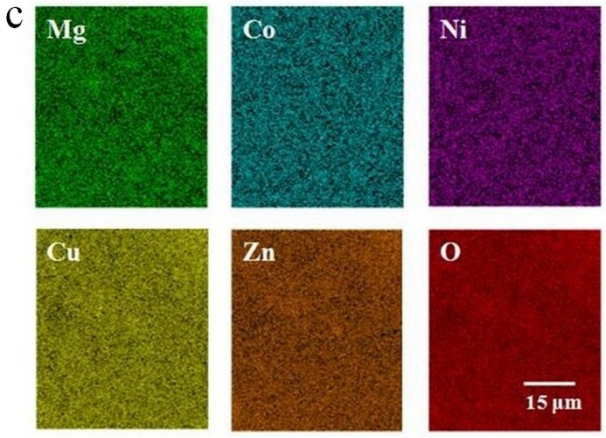
c
Mg
Co
Ni
Cu
Zn
O
15 µm

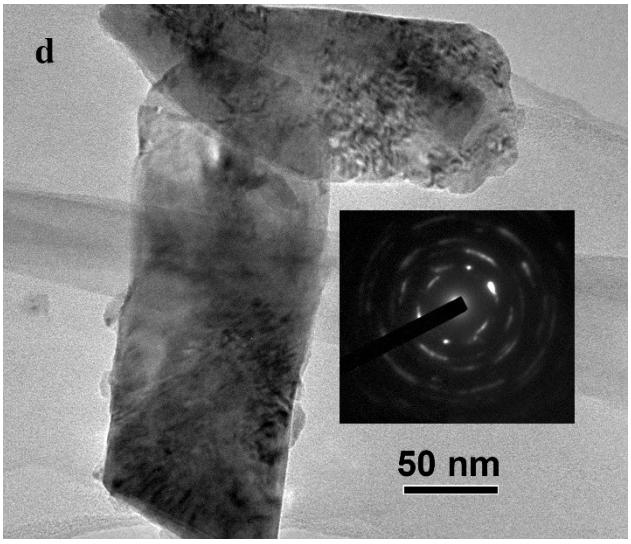


**Figure 1.** X-ray diffraction pattern (a), SEM image (b), EDXS elemental mapping (c) and TEM image/SAED pattern (d) of synthesized $MgCoNiCuZnO_5$ sample. In (a), the X-ray wavelength is 1.5406 Å.

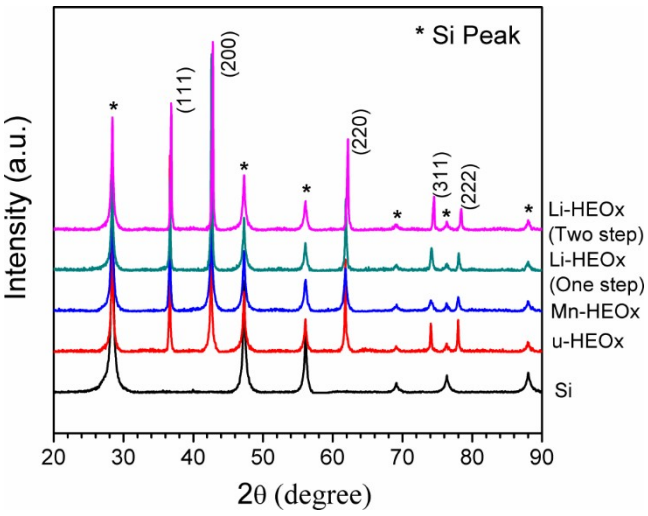


**Figure 2.** X-ray diffraction patterns of u-HEOx, Li-HEOx and Mn-HEOx samples containing Si as an internal 2θ-calibrant for accurately determining the sample lattice parameters. The X-ray wavelength is 1.5406 Å.

### 4.2. Characterization of Li-doped $MgCoNiCuZnO_5$ (Li-HEOx).

The ICP-AES experimental results show that the lithium contents (mass percentages) in the one-step and two-step HEOx samples are, respectively, 0.43 % and 0.69 %. These data confirm that the two-step method indeed produced less lithium loss than the one-step one. Based on these Li contents, the nominal formula of the one-step Li-HEOx is $(Mg,Co,Ni,Cu,Zn)_{0.95}Li_{0.05}O_{0.975}$ and that of the two-step Li-HEOx is $(Mg,Co,Ni,Cu,Zn)_{0.93}Li_{0.07}O_{0.965}$. The first formula coincides with the ideal one without lithium loss (see above) possibly due to slight overestimation of the Li content by the ICP-AES measurements.

XRD patterns of the Li-HEOx samples synthesized from the two different routes are shown in Figure 3a. It is seen that they are similar to that of the u-HEOx, indicating that Li has been doped into the cation sublattice of the rocksalt structure, in agreement with the results from previous works[4, 13]. From Rietveld fitting of the XRD patterns using Si as the internal $2\theta$ calibrant (Figure 2), the lattice parameters *a* of the samples prepared from the one-step and two-step routes are, respectively, 4.233 $\pm$ 0.003 Å and 4.218 $\pm$ 0.007 Å. Both values are smaller than that of the undoped HEOx (4.238 Å; see above).

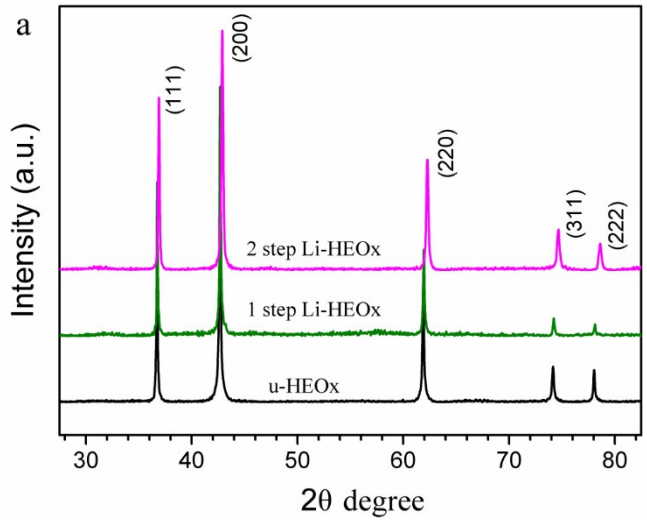
a
Intensity (a.u.)
(111)
(200)
(220)
(311)
(222)
2 step Li-HEOx
1 step Li-HEOx
u-HEOx
30
40
50
60
70
80
2θ degree

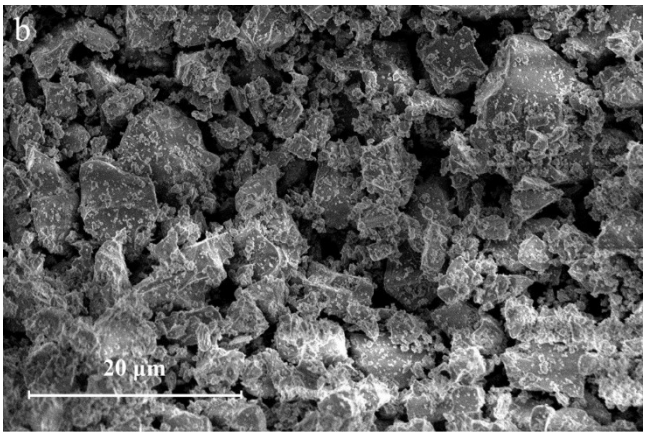
b
20 µm

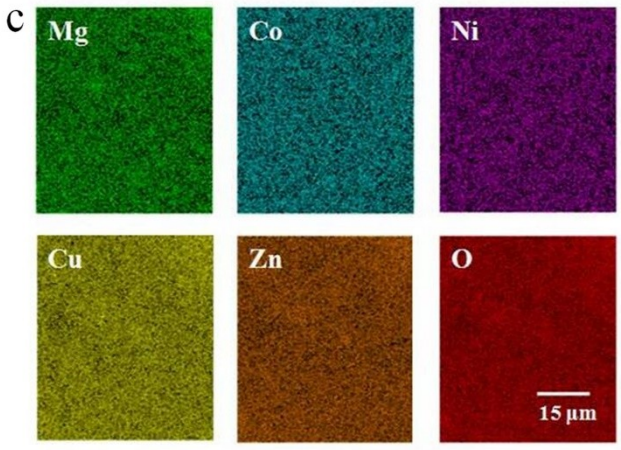
c
Mg
Co
Ni
Cu
Zn
O
15 µm

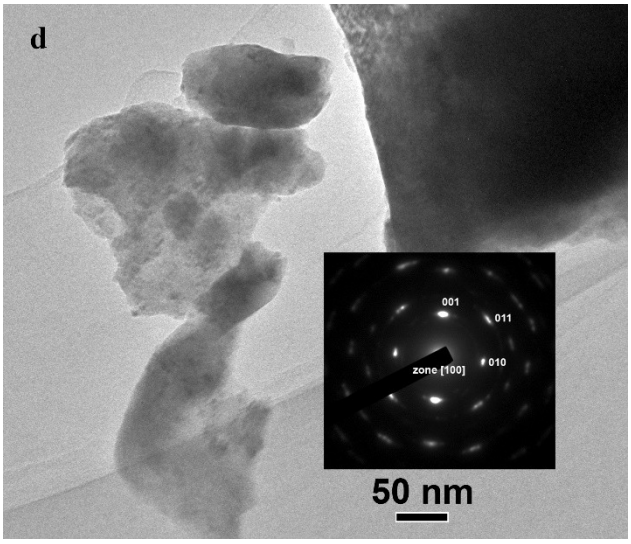


**Figure 3.** X-ray diffraction patterns of Li-doped HEOx prepared from two synthesis routes (a), and SEM image (b), EDXS elemental mapping (c) and TEM image/SAED pattern (d) of the 2-step Li-HEOx. The XRD pattern of the undoped HEOx is included in (a) for comparison. The X-ray wavelength is 1.5406 Å.

The ionic radius in an octahedra coordination of $Li^+$ (0.90 Å)[25] is close to those of other divalent cations - $Mg^{2+}$: 0.86 Å, $Co^{2+}$: 0.79 Å (low spin) or 0.885 Å (high spin), $Ni^{2+}$:0.83 Å, $Cu^{2+}$: 0.87 Å and $Zn^{2+}$:0.88 Å.[25] Thus, substitution of those divalent cations by $Li^+$ ions is feasible. However, substitution of one divalent cation by one monovalent $Li^+$ cation produces one negative charge around the cation site. Two of such substitutions then would require creation of one oxygen vacancy (

$V_O^{\cdot\cdot}$ that carries +2 charges) in the anion sublattice in order to reach charge neutrality in the whole crystal. Thus, considering the requirement of charge neutrality and possible Li loss at a high temperature, the nominal formula of the synthesized Li-doped HEOx should be written as $(Mg,Co,Ni,Cu,Zn)_{0.95}Li_{0.05-x}O_{0.975-0.5x}$, where x represents the Li loss due to volatilization. According to ref. 26, charged oxygen vacancies can cause lattice contraction of original undoped HEOx and hence the lattice parameters *a* of Li-HEOx should be smaller than that of the former, explaining our results above. The *a* value of the two-step Li-HEOx is smaller than that of the one-step Li-HEOx, indicating that more Li has been doped into the cation sublattice in the former than the latter, consistent with the ICP-AES results (see above).

Figures 3b,3c&3d show, respectively, the SEM image, EDXS element mapping and TEM image/SAED pattern of the two-step Li-HEOx sample. Additional EDXS elemental mapping at a relatively high resolution is shown in Figure S3 (SI). All these data shown that, similar to the u-HEOx, the prepared sample is polycrystalline and the constituent elements are uniformly distributed in the sample.

### 4.3. Characterization of Mn-doped $MgCoNiCuZnO_5$ (Mn-

**HEOx).** Figure 4a shows the XRD patterns of the synthesized Mn-HEOx samples. It is seen that the samples synthesized at 1100 and 1300 °C contained secondary phases in addition to the major rocksalt phase. However, when the synthesis temperature was 1500 °C, a single rocksalt phase formed. Thus, the single-phase formation temperature is ~ 400 °C higher than that of the u-HEOx (~ 1100 °C), suggesting that introduction of $Mn^{2+}$ to the undoped HEOx may have increased the formation enthalpy and hence it needs a higher temperature to form a single-phase Mn-HEOx. The increased formation enthalpy was confirmed by our molecular static calculations (see Table 1 below). From Rietveld fitting of the XRD pattern with Si as the internal $2\theta$ calibrant (Figure 2), the lattice parameter of the sample prepared at 1500 °C was obtained: $a$ = 4.237 ± 0.005 Å. The ionic radius of $Mn^{2+}$ is 0.81 Å (low spin) or 0.97 Å (high spin)[25], close to those of other cations (see above). As a result, there should be no significant change in the dimension of the cation sublattice of HEOx after occupation of some cation sites by $Mn^{2+}$. Thus, $a$ of Mn-HEOx (4.237 Å) is close to that of the undoped HEOx (4.238 Å).

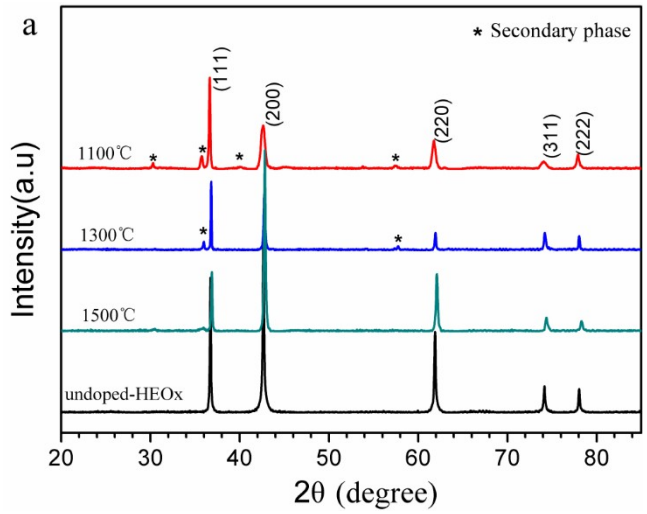
a
* Secondary phase
(111)
(200)
(220)
(311)
(222)
1100℃
1300℃
1500℃
undoped-HEOx
Intensity(a.u)
20
30
40
50
60
70
80
2θ (degree)

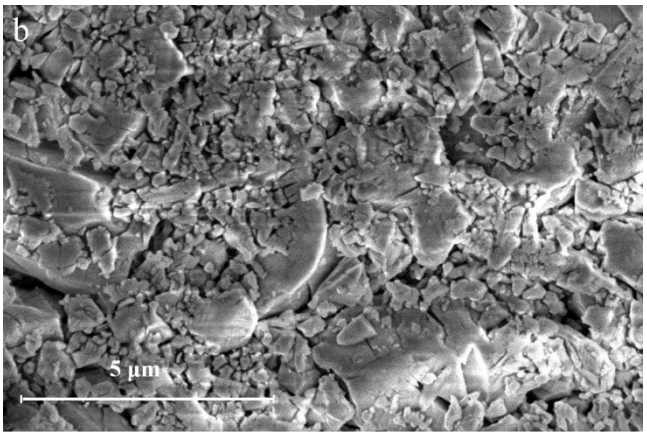
b
5 μm

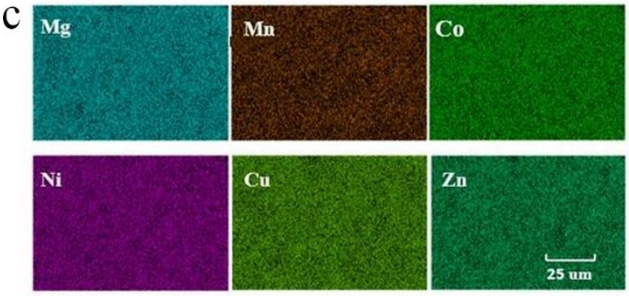
c
Mg
Mn
Co
Ni
Cu
Zn
25 um

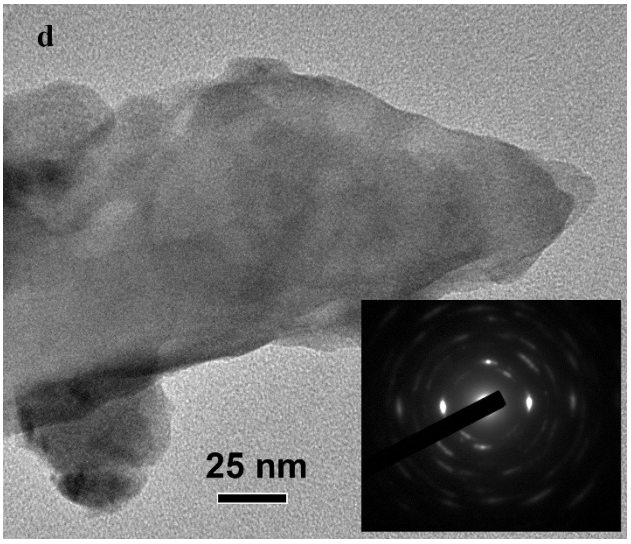


**Figure 4.** XRD patterns of Mn-doped HEOx synthesized at different temperatures (a), and SEM image (b), EDXS elemental mapping (c) and TEM image/SAED pattern (d) of the sample synthesized at 1500 ℃. The XRD pattern of undoped HEOx is included for comparison in (a). The X-ray wavelength is 1.5406 Å.

The SEM image of the Mn-HEOx sample synthesized at 1500 ºC (Figure 4b) reveals that the synthesized sample contains lots of micron-sized grains. The EDXS elemental mapping of the sample (Figure 4c; Figure S4 at a relatively high resolution in the SI) shows that there are no spatial enrichment or clustering of cations in the sample, indicating uniform distribution of the elements in the sample. The SAED pattern (Figure 4d) shows that the very fine sample particles are crystalline. Thus, the experimental data shown in Figures 4a, 4b & 4d reveal the

fact that the synthesized Mn-HEOx sample is polycrystalline and in the rocksalt structure.

**4.4. Thermal stability of undoped and doped HEOx.** The free energy of formation ($\Delta G$) of a high-entropy oxide from its constituent simple oxides is

$$\Delta G = \Delta H - T\Delta S \quad (2)$$

where $\Delta H$ and $\Delta S$ are, respectively, the enthalpy of formation and entropy of formation from the simple oxides. Previous thermal analysis experiment showed that $\Delta H > 0$ for $MgCoNiCoZnO_5$.[1] Our MS calculation results (Table 1) show that the formation enthalpies of undoped and doped HEOx are all above zero, i.e., $\Delta H(0\ K) > 0$. Assuming that the experimental $\Delta H$ is dominated by the potential energy (due to atomic interactions) rather than the kinetic energy (due to thermal vibrations), the predicted $\Delta H(0\ K) > 0$ is consistent with the experimental $\Delta H > 0$ in ref. 1. Moreover, Table 1 shows that the formation enthalpy of the HEOx increases after doping. This can be attributed to the introduction of Li/Mn-O bonds to the HEOx, as they are weaker in the bond strength (characterized by the magnitude of the lattice energy of MeO; Table 1) than other cation-O bonds in the u-HEOx (except that Mn-O and Cu-O bonds have similar strengths), making a doped HEOx possessing a higher enthalpy. Peculiarly, the formation energy of Li-HEOx is much

higher than that of Mn-HEOx. This arose because O vacancies were treated as distributing randomly in the anion sublattice of Li-HEOx in the MS calculations. More realistically, O vacancies should be preferably distributed near Li-doping sites in order to reduce the total system energy, since the electrostatic repulsion between a $V_O^{\cdot\cdot}$ and a nearby $Li^+$ ion is lower than that between a $V_O^{\cdot\cdot}$ and a nearby $Me^{2+}$ ion. We will use molecular dynamics simulations to treat this scenario in a future work.

For a high-entropy oxide at high temperature, its entropy comes mainly from the configurational entropy due to random distribution of cations in the cation sublattice.[1] Thus, for one molar HEOx (e.g., (Mg,Co,Ni,Cu,Zn)O for the u-HEOx), the molar entropy change $\Delta S \approx -R\Sigma x_i \ln x_i$, where R represents the universal gas constant (8.314 J $mol^{-1}$ $K^{-1}$) and $x_i$ is the molar fraction of a constituent simple oxide. Using this approximation, $\Delta S$ = 13.4 and 14.4 J $mol^{-1}$ $K^{-1}$ for u-HEOx and Li/Mn-HEOx, respectively. Then, according to equation 2, high-extropy oxides are thermodynamically stable (i.e., $\Delta G \leq 0$) only at temperatures higher than a formation temperature $T_f = (\Delta H/\Delta S) > 0$. Our synthesis experiments show that $T_f \geq \sim$ 1100, 1100 and 1500 °C for the u- HEOx,

Li-HEOx and Mn-HEOx, respectively (see above). Based on this, we deduce that $\Delta H(Mn\text{-}HEOx) > \Delta H(u\text{-}HEOx \text{ or } Li\text{-}HEOx) > 0$. This supports our MS-derived results in Table 1: $\Delta H(Mn\text{-}HEOx, 0K) > \Delta H(u\text{-}HEOx, 0\ K)$.

**Table 1. Lattice Parameters, Bulk Moduli and Lattice Energies of Simple and High-Entropy Oxides Obtained from Molecular Static Calculations**

| Oxide | *a* (Å) | *b* (Å) | *c* (Å) | $\beta$ or $\gamma$ (°) | $B_0$(GPa) Calc. | $B_0$(GPa) Expt./ Lit. | $E_{latt.}$ (kJ mol$^{-1}$) | $\Delta H(0\ K)$ (kJ mol$^{-1}$) | Ref. for $B_0$ |
|---|---|---|---|---|---|---|---|---|---|
| CoO (cubic) | 4.245 (4.263)[a] | | | | 194.7 | 190.5 | 3859.01 (3910)[14] | | 27 |
| CuO (mono.) | 5.138 (4.683)[b] | 3.730 (3.429)[b] | 5.138 (5.130)[b] | 86.9 (99.3)[b] | 110.0 | 73.9 98 | 3669.18 (4050)[14] | | 28 29 |
| CuO (cubic)[c] | 4.373 [c] | | | | 148.6 | | 3665.60 | | |
| $Li_2O$ (cubic) | 4.523 (4.612 | | | | 103.6 | 93.6 78.0 | 2932.00 | | 30 31 |

| | | | | | | | | | |
|---|---|---|---|---|---|---|---|---|---|
| | )[d] | | | | | | (2814) [14] | | |
| MgO (cubic) | 4.134 (4.208 )[e] | | | | 156.2 | 160 – 163 156, 178 | 4388.44 (3791) [14] | | 27 27 |
| MnO (cubic) | 4.437 (4.446 )[f] | | | | 158.8 | 155.1 149 – 153 144, 162 | 3678.03 (3745) [14] | | 32 27 27 |
| NiO (cubic) | 4.179 (4.183 )[g] | | | | 202.9 | 205 199 | 3908.86 (4010) [14] | | 27 27 |
| ZnO (hex.) | 3.268 (3.242 )[h] | 3.268 (3.242 ) | 5.074 (5.188 ) | 120 | 144.7 | 143.5 183 | 3851.18 (3971) [14] | | 27 33 |
| ZnO (cubic) | 4.267 (4.28)[i] | | | | 192.0 | 170 228 | 3842.57 | | 34 33 |
| u-HEOx (cubic) | 4.241 (4.238 )[j] | | | | 185.8 (178.9) [k] | 187.7 [j] | 3929.83 | 3.07 [l] 5.51 [m] | This work |
| Li- | 4.235 | | | | 176.8 | | 3736.9 | 72.60 [l,n] | |

| | | | | | | | | | |
|---|---|---|---|---|---|---|---|---|---|
| HEOx (cubic; 1-step) | (4.233)[j] | | | | (175.1)[k] | | 5[n] | 74.91[m,n] | |
| Li-HEOx (cubic; 2-step) | 4.233 (4.218)[j] | | | | 173.2 (173.6)[k] | 156.2[j] | 3661.17[n] | 99.04[l,n] 101.31[m,n] | This work |
| Mn-HEOx (cubic) | 4.251 (4.237)[j] | | | | 184.8 (177.9)[k] | 162.2[j] | 3916.26 | 3.89[i] 6.21[m] | This work |

[a] COD (Ref. 35) #1533087; [b] COD #9015924; [c] fictious cubic structure; [d] COD #4121515; [e] COD #9000499; [f] COD #9005946; [g] COD #4320487; [h] COD #2107059; [i] COD #1534836; [j] expt. from present work; [k] molar fraction weighted-sum of MS-derived $B_0$ of simple oxides (cubic); [l] $\Delta H(0\ K)$ from cubic simple oxides; [m] $\Delta H(0\ K)$ from most stable simple oxides; [n] values for Li-HEOx were highly overestimated due to treating O vacancy as randomly distributed in the anion sublattice in the MS calculations (see text).

As high entropy oxides are thermodynamically stable only at temperatures higher than $T_f$, at lower temperatures they become thermodynamically unstable and thus may decompose into simple oxides (or fewer-component complex oxides), subject to attainable

kinetics at given temperatures. With this consideration, we investigated the thermal stabilities of undoped and Li/Mn-doped HEOx using in-situ XRD. The experimental results (Figure 5) show that on heating the samples from RT to 450 $^{o}$C in a flowing nitrogen gas, no phase decompositions were observed. Thus, the HEOx compounds are thermally stable at the experimental conditions. These results suggest that the activation energies for the decompositions of the HEOx compounds to constituent simple oxides are relatively high. In a decomposition reaction of HEOx, it is necessary to break and rearrange different kinds of metal cation-O bonds via migrations of cations from a randomly distributed HEOx cation sublattice to several orderly distributed cation sublattices of the constituent simple oxides. These factors make the decomposition reaction difficult at relatively low temperatures.

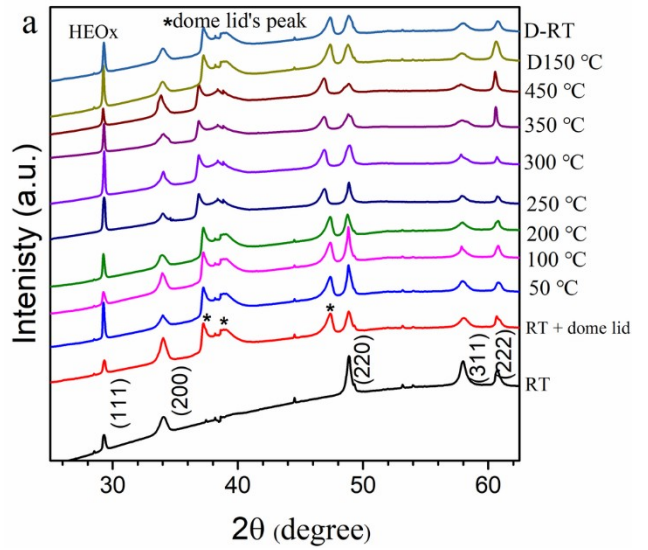
a
HEOx
*dome lid's peak
D-RT
D150 ℃
450 ℃
350 ℃
300 ℃
250 ℃
200 ℃
100 ℃
50 ℃
RT + dome lid
RT
(111)
(200)
(220)
(311)
(222)
Intenisty (a.u.)
2θ (degree)

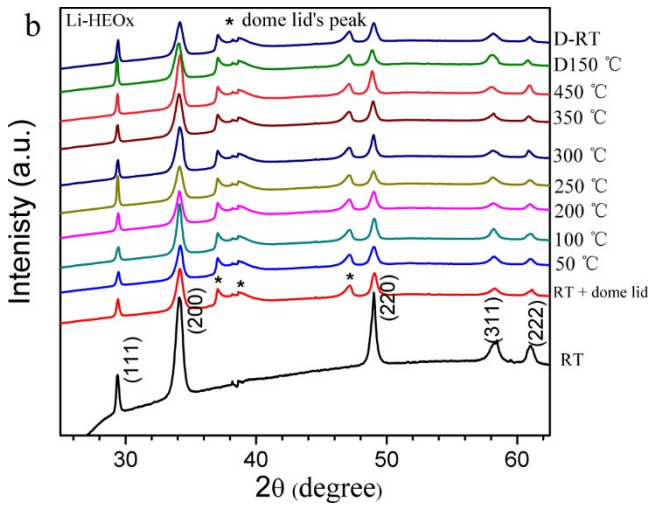
b
Li-HEOx
* dome lid's peak
D-RT
D150 ℃
450 ℃
350 ℃
300 ℃
250 ℃
200 ℃
100 ℃
50 ℃
RT + dome lid
RT
(111)
(200)
(220)
(311)
(222)
Intenisty (a.u.)
2θ (degree)

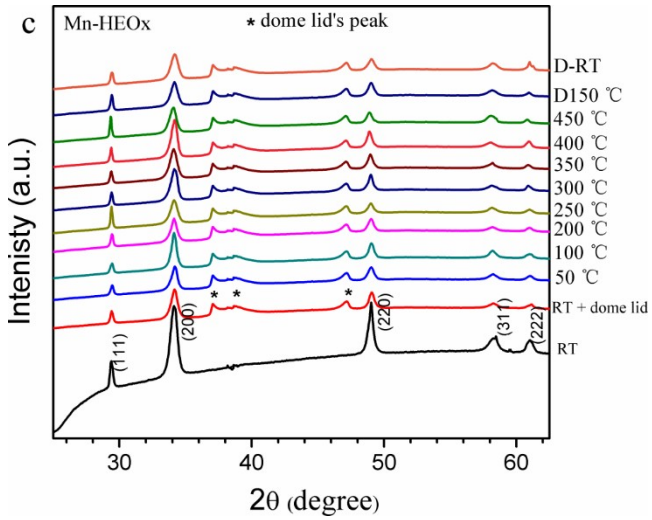
c
Mn-HEOx
* dome lid's peak
D-RT
D150 ℃
450 ℃
400 ℃
350 ℃
300 ℃
250 ℃
200 ℃
100 ℃
50 ℃
RT + dome lid
RT
(111)
(200)
(220)
(311)
(222)
Intenisty (a.u.)
2θ (degree)

**Figure 5.** In-situ XRD patterns of u-HEOx (a), Li-HEOx (b) and Mn-HEOx (c) on heating from RT to 450 °C in flowing nitrogen gas (X-ray wavelength 1.2400 Å). Prefix “D” prior to a temperature value denotes cooling; “*” symbols indicate diffraction peaks from the dome lid of the heating stage. The very bottom XRD pattern in each diagram was collected at RT without enclosing the dome lid onto the heating stage.

**4.5. Mechanical stability and elasticity of undoped and doped HEOx.** High-pressure XRD patterns of the undoped HEOx (in neon pressure medium) and the Li/Mn-doped HEOx (in methanol-ethanol medium) are shown in Figure 6. It is seen that no phase transitions occurred in all the HEOx at pressures up to ~ 50 GPa at room temperature (further confirmed by repeated HP-XRD measurements of the latter two; see Figure S5 in the SI). By comparison, some constituent simple oxides undergo pressure-induced phase transitions at P < 50 GPa. For instance, CoO and MnO change from a cubic to a rhombohedral structure at 37 and 40 GPa, respectively,[36] and ZnO from a hexagonal to a cubic structure at ~ 9 GPa.[37] We infer that the random cation distribution in the cation sublattice of a HEOx increases more the free energy of a potential high-pressure phase than the ambient cubic phase, which widens the

phase stability of the cubic phase and hence no phase transitions occurred in the HEOx in our experimental pressure range. Thus, all the undoped and Li/Mn-doped HEOx compounds are quite mechanically stable at room temperature (at P up to ~ 50 GPa). The relatively high thermal and mechanical stabilities of HEOx facilitate development of versatile applications in wide ranges of temperature and pressure.

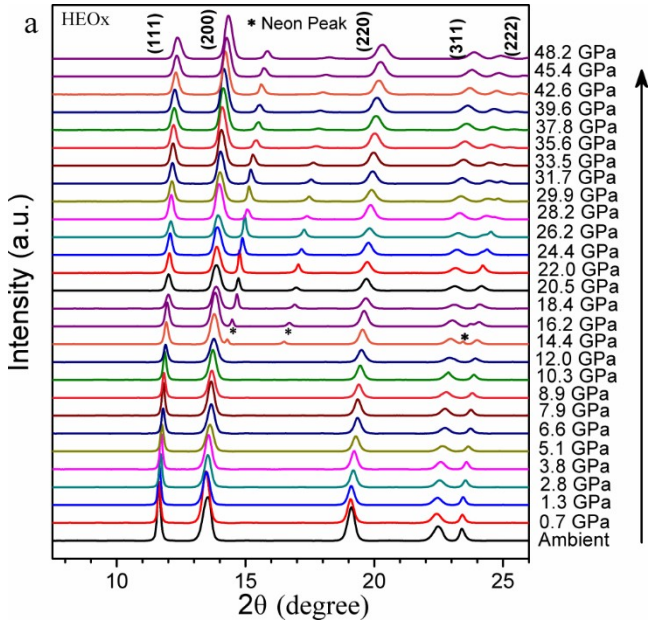

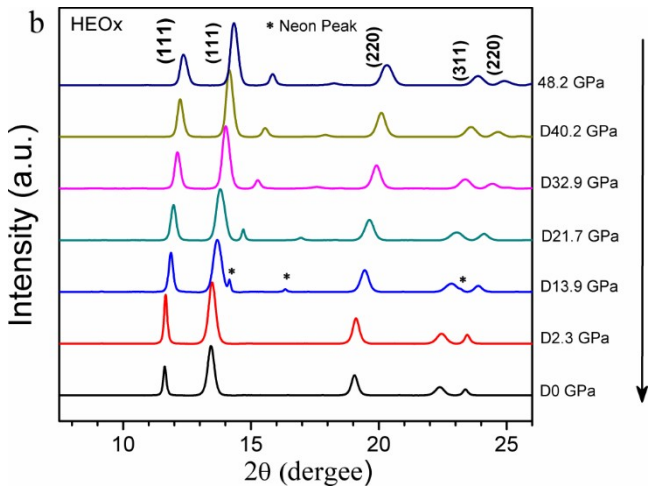
b
HEOx
* Neon Peak
(111)
(111)
(220)
(311)
(220)
48.2 GPa
D40.2 GPa
D32.9 GPa
D21.7 GPa
D13.9 GPa
D2.3 GPa
D0 GPa
Intensity (a.u.)
10
15
20
25
2θ (dergee)

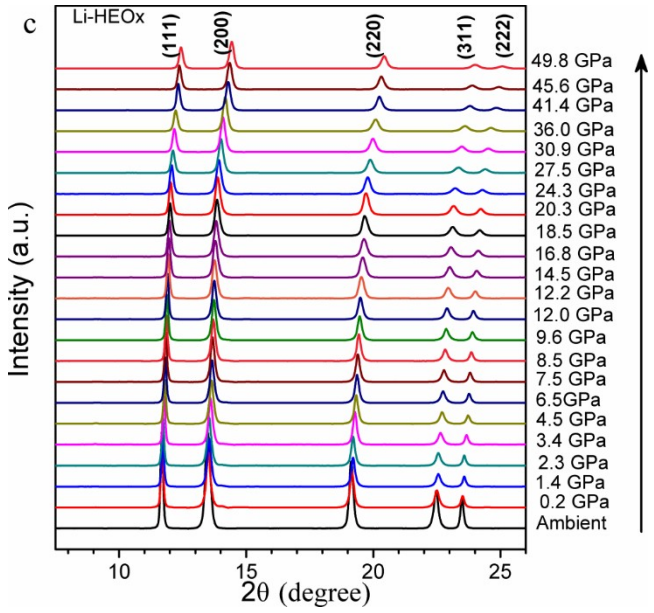
c
Li-HEOx
(111)
(200)
(220)
(311)
(222)
49.8 GPa
45.6 GPa
41.4 GPa
36.0 GPa
30.9 GPa
27.5 GPa
24.3 GPa
20.3 GPa
18.5 GPa
16.8 GPa
14.5 GPa
12.2 GPa
12.0 GPa
9.6 GPa
8.5 GPa
7.5 GPa
6.5GPa
4.5 GPa
3.4 GPa
2.3 GPa
1.4 GPa
0.2 GPa
Ambient
Intensity (a.u.)
10
15
20
25
2θ (degree)

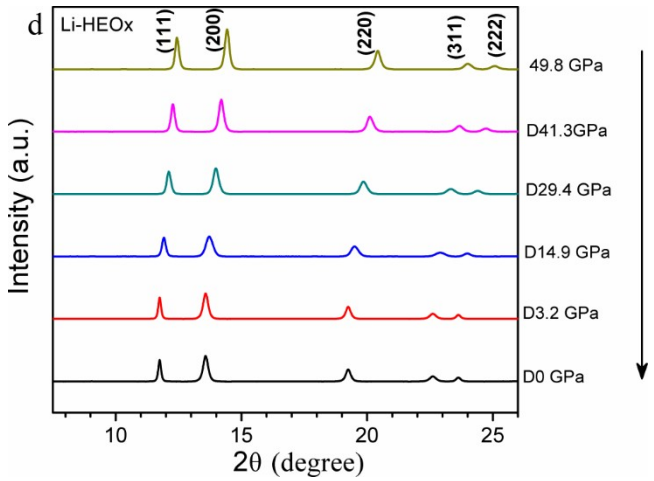
d
Li-HEOx
(111)
(200)
(220)
(311)
(222)
49.8 GPa
D41.3GPa
D29.4 GPa
D14.9 GPa
D3.2 GPa
D0 GPa
Intensity (a.u.)
10
15
20
25
2θ (degree)

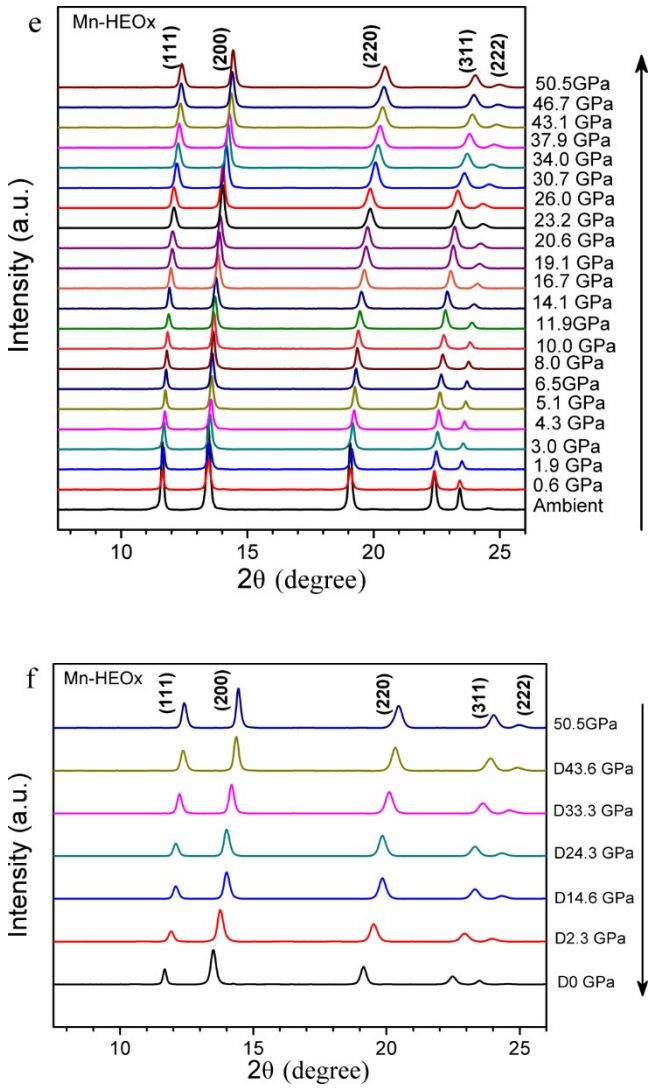


**Figure 6.** High pressure XRD patterns of u-HEOx in neon medium (a, b), Li-HEOx in methanol-ethanol medium (c, d), and Mn-HEOx in methanol-ethanol medium (e, f) in compression (a, c, e) and decompression (b, d, f) at room temperature. X-ray wavelength is 0.4959 Å. In (a) and (b), "*" markers indicate diffraction peaks from neon.

Again, we used the periclase phase of MgO as the structure model to perform Rietveld fitting of the HP-XRD data of undoped and Li/Mn-doped HEOx (Figure 6) in order to obtain their pressure-dependent lattice parameters and hence the unit cell volumes. Figure S6 (SI) illustrates representative Rietveld fittings at chosen pressures. The obtained unit cell volumes as a function of pressure are shown in Figure 7.

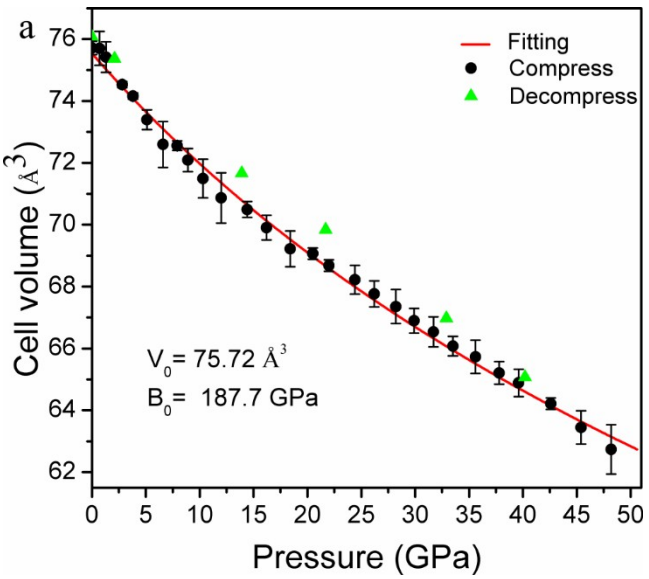

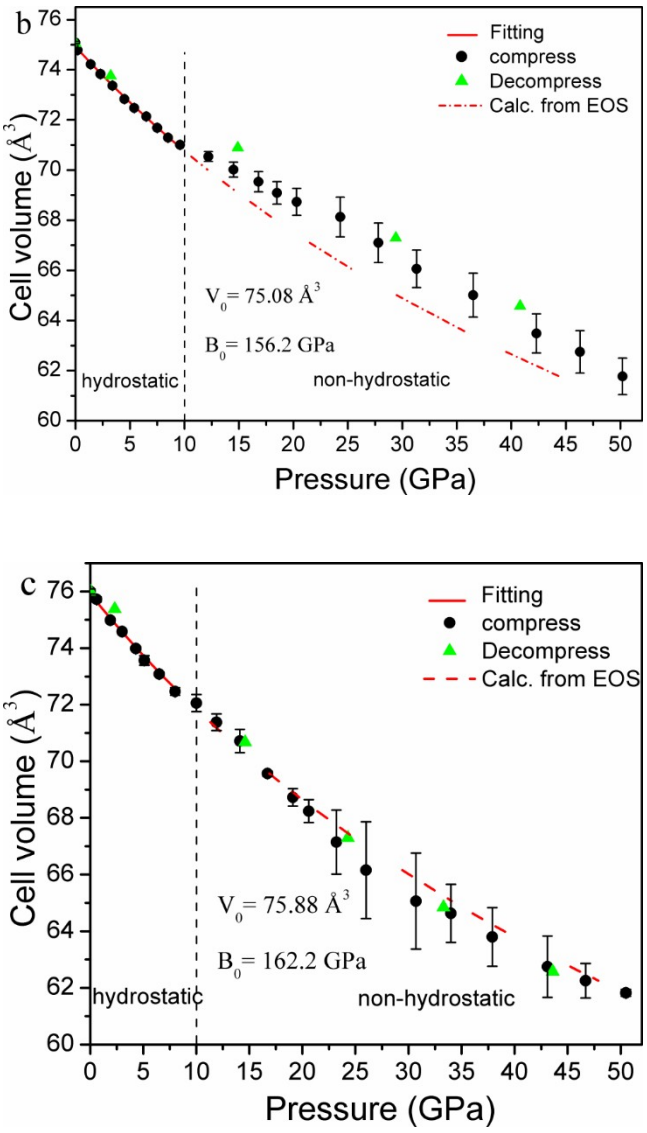


**Figure 7.** Variations of unit cell volumes (descripted using a Fm$\bar{3}$m space group) of u-HEOx (a), two-step Li-HEOx (b) and Mn-HEOx (c) as a function of pressure. Lines are fits to the experimental data using the third-order Birch−Murnaghan equation of state.

We then used the third-order Birch−Murnaghan equations of state

(EOS)[38] to fit the unit cell volume *vs* pressure data shown in Figure 7:

$$P(V)=1.5B_0\left[\left(\frac{V_0}{V}\right)^{7/3}-\left(\frac{V_0}{V}\right)^{5/3}\right]\bullet\left\{1+\frac{3}{4}(B_0^{'}-4)\left[(\frac{V_0}{V})^{2/3}-1\right]\right\} \qquad (3)$$

where $P$ is the pressure, $B_0$ is the bulk modulus, $B_0^{'}$ is the pressure derivative of the bulk modulus, ¿$V_0$ and $V$ are the unit cell volumes at ambient pressure and pressure $P$, respectively. In fitting the experimental data to the EOS above, $B_0^{'}$ is commonly fixed at 4.0 GPa.[39] Rigorously, equation 3 is applicable only to systems at hydrostatic conditions.

It has been shown that, the neon pressure medium can produce hydrostatic and quasi-hydrostatic conditions at P up to ~ 50 GPa, while methanol-ethanol medium can only produce hydrostatic conditions at P up to ~ 10.5 GPa.[40] Thus, in our fitting of the experimental data to equation 3, all compression data points in Figure 7a and those below 10 GPa in Figures 7b & 7c were used, as done in a previous work.[41] Decompression data points were not included in the fittings due to their apparent deviations from the compression data, which are more

apparent in the neon medium (Figure 7a) possibly due to continuous structure relaxation of the HEOx while subjecting to X-ray diffraction. The fit results are shown in Figure 7 and the obtained bulk moduli are: $B_0$(u-HEOx) = 187.7 ± 3.5 GPa, $B_0$(2-step Li-HEOx) = 156.2 ± 2.8 GPa and $B_0$(Mn-HEOx) = 162.2 ± 5.9 GPa.

**4.6. Understanding doping effect on compressibility of high-entropy oxides using MS calculations.** Above experimental results show that Li/Mn-doping causes decrease in the bulk modulus of HEOx, making HEOx more compressible (i.e., softer). Under compression, the Me-O bond length of a MeO compound shortens, causing increase in the internal energy. A MeO compound with stronger Me-O bonds can resist more the compression, producing a higher bulk modulus. Thus, a decrease in the bulk modulus of HEOx after doping suggests a weakening in the Me-O bond, as verified by our MS calculations (below).

For ionic crystals, the strength of ionic interactions (or ionic bond strength) can be characterized by the lattice energy.[42] Our MS-derived bulk moduli and lattice energies of concerned simple and high-entropy oxides are listed in Table 1. It is seen that the calculated bulk moduli agree fairly well with available literature and/or experimental data. The

calculated lattice energies also agree fairly well with those derived from the Born–Fajans–Haber cycle. [14] These illustrate that the MS calculations describe consistently and reasonably well the atomic interactions in both the simple and high-entropy oxides, giving that no any level of quantum mechanical treatments were employed. Table 1 shows that, for the undoped and Li/Mn-doped HEOx, their molar fraction weighted-sum of the bulk moduli of constituent simple oxides are close to the MS-derived values (though the former underestimate the latter to some degrees), suggesting that all kinds of Me-O bonds in a HEOx resist external compression cooperatively.

As seen from Table 1, both the $B_0$ and the magnitude of $E_{latt}$ of $LiO_{0.5}$ (1/2 $Li_2O$) are smaller than those of other constituent oxides, indicating that Li-O bonds are weaker than other Me-O bonds in our concerned oxides. Thus, the experimentally observed lower bulk modulus of Li-HEOx than u-HEOx (Table 1) can be attributed to the introduction of the less strong Li-O bonds to the HEOx structure.

Although the $B_0$ of MnO is close to those of cubic CuO and MgO, it is smaller than those of cubic CoO, NiO and ZnO (Table 1). The magnitude of $E_{latt}$ of MnO is comparable to that of cubic CuO, but smaller than those of cubic MgO, CoO, NiO and ZnO (Table 1). Thus, the average

strength of all the Me-O bonds in Mn-HEOx should be smaller than that in u-HEOx due to introduction of Mn-O bonds to the HEOx structure. As a result, the $B_0$ of Mn-HEOx should be smaller than that of u-HEOx, as confirmed by the experimental results (Table 1).

Because the $B_0$ (103.6 GPa) and the magnitude of $E_{latt}$ (1466.00 kJ $mol^{-1}$) of $LiO_{0.5}$ are smaller than the $B_0$ (156.2 GPa) and the magnitude of $E_{latt}$ (3678.02 kJ $mol^{-1}$) of MnO, respectively, the $B_0$ of Li-HEOx should be smaller than that of Mn-HEOx, as confirmed by both the MS and experimental results (Table 1). Overall, the MS calculations predict $B_0$(Li-HEOx) < $B_0$(Mn-HEOx) < $B_0$(u-HEOx) as a consequence of increasing average bond strength of the Me-O bonds in these oxides, consistent with the HP-XRD results (Table 1). Based on above discussions, we argue that the doping-induced elastic softening of HEOx arises from introduction of weaker Li-O or Mn-O bonds in the high-entropy compound.

## 5. CONCLUSION

In this work, we have prepared undoped and Li- and Mn-doped high-entropy oxides using solid-state reactions at high temperatures. In-situ heating and compression synchrotron XRD experimental results show

that these HEOx compounds are thermally stable at T up to ~ 450 °C and mechanically stable at P up to ~ 50 GPa. High-pressure XRD experimental results show that doping of Li and Mn makes the HEOx more compressible because of the introduction of Li-O or Mn-O ionic interactions that are weaker than other cation-O interactions, as revealed by molecular static calculations. The formation reaction of a HEOx was predicted as endothermic by the MS calculations, consistent with reported experimental data. This work provides us new understanding on the relationship between the structure modification and mechanical property change in HEOx via doping, and will have important implications to new HEOx material design, syntheses and application development.

## ASSOCIATED CONTENT

### Supporting Information

The Supporting Information is available free of charge on the ACS Publications website at DOI:

Derivation of interatomic potential functions, additional EDXS elemental mapping data, additional high-pressure XRD patterns, representative Rietveld fitting.

## AUTHOR INFORMATION


### Corresponding Authors

* E-mail: hengzhong.zhang@hpstar.ac.cn, Phone: +86-21-80177095.

* E-mail: zlyin_csu@163.com.

ORCID

Jian Chen: 0000-0002-6837-2551

Hengzhong Zhang: 0000-0003-2322-2274


# Notes

The authors declare no competing financial interest.

## ACKNOWLEDGMENTS

This research was supported by the National Natural Science Foundation of China (grant # 21875005). The research used resources of the Advanced Light Source (ALS), Berkeley, California, USA. ALS is a US DOE Office of Science User Facility under contract no. DE-AC02-05CH11231. The high-pressure synchrotron X-ray diffraction was conducted at the high energy beamline station ALS-12.2.2; the in-situ heating X-ray diffraction was conducted at the micro-XRD station ALS-12.3.2. We thank Yanping Yang for assistance with SEM sample characterization and Hongliang Dong for help on sample preparations.

## REFERENCES

(1) Rost, C. M.; Sachet, E.; Borman, T.; Moballegh, A.; Dickey, E. C.; Hou, D.; Jones, J. L.; Curtarolo, S.; Maria, J. P. Entropy-Stabilized Oxides. *Nat. Commun.* **2015**, *6*, 8485.

(2) Sarkar, A.; Velasco, L.; Wang, D.; Wang, Q.; Talasila, G.; de Biasi, L.; Kubel, C.; Brezesinski, T.; Bhattacharya, S. S.; Hahn, H. et al. High Entropy Oxides for Reversible Energy Storage. *Nat. Commun.* **2018**, *9*, 3400.

(3) Chen, H.; Fu, J.; Zhang, P.; Peng, H.; Abney, C. W.; Jie, K.; Liu, X.; Chi, M.; Dai, S. Entropy-Stabilized Metal Oxide Solid Solutions as CO Oxidation Catalysts with High-Temperature Stability. *J. Mater. Chem. A* **2018**, *6*, 11129-11133.

(4) Bérardan, D.; Franger, S.; Meena, A. K.; Dragoe, N. Room Temperature Lithium Superionic Conductivity in High Entropy Oxides. *J. Mater. Chem. A* **2016**, *4*, 9536-9541.

(5) Zhai, S.; Rojas, J.; Ahlborg, N.; Lim, K.; Toney, M. F.; Jin, H.; Chueh, W. C.; Majumdar, A. The Use of Poly-Cation Oxides to Lower the Temperature of Two-Step Thermochemical Water Splitting. *Energ. Environ. Sci.* **2018**, *11*, 2172-2178.

(6) Jiang, S.; Hu, T.; Gild, J.; Zhou, N.; Nie, J.; Qin, M.; Harrington, T.; Vecchio, K.; Luo, J. A New Class of High-Entropy Perovskite Oxides.

*Scripta Mater.* **2018**, *142*, 116-120.

(7) Sarkar, A.; Djenadic, R.; Wang, D.; Hein, C.; Kautenburger, R.; Clemens, O.; Hahn, H. Rare Earth and Transition Metal Based Entropy Stabilised Perovskite Type Oxides. *J. Eur. Ceram. Soc.* **2018**, *38*, 2318-2327.

(8) Gild, J.; Samiee, M.; Braun, J. L.; Harrington, T.; Vega, H.; Hopkins, P. E.; Vecchio, K.; Luo, J. High-Entropy Fluorite Oxides. *J. Eur. Ceram. Soc.* **2018**, *38*, 3578-3584.

(9) Djenadic, R.; Sarkar, A.; Clemens, O.; Loho, C.; Botros, M.; Chakravadhanula, V. S. K.; Kübel, C.; Bhattacharya, S. S.; Gandhi, A. S.; Hahn, H. Multicomponent Equiatomic Rare Earth Oxides. *Mater. Res. Lett.* **2016**, *5*, 102-109.

(10) Sarkar, A.; Loho, C.; Velasco, L.; Thomas, T.; Bhattacharya, S. S.; Hahn, H.; Djenadic, R. Multicomponent Equiatomic Rare Earth Oxides with a Narrow Band Gap and Associated Praseodymium Multivalency. *Dalton Trans.* **2017**, *46*, 12167-12176.

(11) Dąbrowa, J.; Stygar, M.; Mikuła, A.; Knapik, A.; Mroczka, K.; Tejchman, W.; Danielewski, M.; Martin, M. Synthesis and Microstructure of the $(Co,Cr,Fe,Mn,Ni)_3O_4$ High Entropy Oxide Characterized by Spinel Structure. *Mater. Lett.* **2018**, *216*, 32-36.

(12) Zhai, T.; Zhao, M.-s.; Wang, D.-d. Effect of Mn-Doping on

Performance of $Li_3V_2(PO_4)_3$/C Cathode Material for Lithium Ion Batteries. *Trans. Nonferrous Met. Soc. China* **2011**, *21*, 523-528.

(13) Bérardan, D.; Franger, S.; Dragoe, D.; Meena, A. K.; Dragoe, N. Colossal Dielectric Constant in High Entropy Oxides. *Phys. Status Solidi-R* **2016**, *10*, 328-333.

(14) Lide, D. R. *CRC Handbook of Chemistry and Physics, 86th Edition;* CRC Press: Boca Raton, FL, 2005.

(15) Rost, C. M. Entropy-Stabilized Oxides Explorations of a Novel Class of Multicomponent Materials. Ph.D. Dissertation, North Carolina State University, Raleigh, NC, 2016.

(16) Rak, Z.; Rost, C. M.; Lim, M.; Sarker, P.; Toher, C.; Curtarolo, S.; Maria, J. P.; Brenner, D. W. Charge Compensation and Electrostatic Transferability in Three Entropy-Stabilized Oxides: Results from Density Functional Theory Calculations. *J. Appl. Phys.* **2016**, *120*, 095105.

(17) Tamura, N. In *Strain and Dislocation Gradients from Diffraction*; Barabash, R. I., Ice, G. E., Eds.; Imperial College Press: London, U. K., **2014;** pp 125-155.

(18) Kunz, M.; MacDowell, A. A.; Caldwell W. A.; Cambie, D.; Celestre, R. S.; Domning, E. E.; Duarte, R. M.; Gleason, A. E.; Glossinger, J. M.; Kelez, N. et al. A Beamline for High-Pressure Studies at the Advanced Light Source with a Superconducting Bending Magnet as the Source. *J.*

*Synchrotron Radiat.* **2005**, *12*, 650-8.

(19) Hammersley, A. P.; Svensson, S. O.; Hanfland, M.; Fitch, A. N.; Hausermann, D. Two-Dimensional Detector Software: From Real Detector to Idealised Image or Two-Theta Scan. *High Pressure Res.* **1996**, *14*, 235-248.

(20) Toby, B. H. EXPGUI, a Graphical User Interface for GSAS. *J. Appl. Crystallogr.* **2001**, *34*, 210-213.

(21) Lewis, G. V.; Catlow, C. R. A. Potential Models for Ionic Oxides. *J. Phys. C: Solid State Phys.* **1985**, *18*, 1149-1161.

(22) Dick, B. G.; Overhauser, A. W. Theory of the Dielectric Constants of Alkali Halide Crystals. *Phys. Rev.* **1958**, *112*, 90-103.

(23) Gale, J. D. GULP: Capabilities and Prospects. *Z. Kristallogr.* **2005**, *220*, 552-554.

(24) Rietveld, H. M. A Profile Refinement Method for Nuclear and Magnetic Structures. *J. Appl. Crystallogr.* **1969**, *2*, 65-71.

(25) Shannon, R. D. Revised Effective Ionic Radii and Systematic Studies of Interatomie Distances in Halides and Chaleogenides. *Acta Crystallogr. Sect. A* **1976**, *32*, 751-767.

(26) Aidhy, D. S.; Liu, B.; Zhang, Y.; Weber, W. J. Chemical Expansion Affected Oxygen Vacancy Stability in Different Oxide Structures from First Principles Calculations. *Comput. Mater. Sci.* **2015**, *99*, 298-305.

(27) *Mineral Physics and Crystallography: A Handbook of Physical Constants*; Ahrens, T. J., Ed.; American Geophysical Union: Washington, DC, 1995.

(28) Liu, N. N.; Sun, J. L.; Wu, D. Elastic Constants and Thermodynamic Properties of Cu, $Cu_2O$ and CuO from First-Principles Calculations. *Adv. Mater. Res.* **2011**, *335–336*, 328–332.

(29) Årsbrink, S.; Gerward, L.; Olsen, J. S.; Steenstrup, S. High Pressure Studies up to 50 GPa of CuO. *High Pressure Res.* **2006**, *10*, 515-521.

(30) Feng, L. X.; Rong, C. X.; Fu, J. G.; Min, M. C. Ab Initio Calculations of Elastic Constants of $Li_2O$ under Pressure. *Chin. Phys. Lett.* **2006**, *23*, 925-927.

(31) Hull, S.; Farley, T. W. D.; Hayes, W.; Hutchings, M. T. The Elastic Properties of Lithium Oxide and Their Variation with Temperature. *J. Nucl. Mater.* **1988**, *160*, 125-134.

(32) Pacalo, R. E.; Graham, E. K. Pressure and Temperature Dependence of the Elastic Properties of Synthetic MnO. *Phys. Chem. Miner.* **1991**, *18*, 69-80.

(33) Karzel, H.; Potzel, W.; Kofferlein, M.; Schiessl, W.; Steiner, M.; Hiller, U.; Kalvius, G. M.; Mitchell, D. W.; Das, T. P.; Blaha, P. et al. Lattice Dynamics and Hyperfine Interactions in ZnO and ZnSe at High External Pressures. *Phys. Rev.* **1996**, *53*, 11425-11438.

(34) Gerward, L.; Olsen, J. S. The High-Pressure Phase of Zincite. *J. Synchrotron. Rad.* **1995**, *2*, 233-235.

(35) Grazulis, S.; Daskevic, A.; Merkys, A.; Chateigner, D.; Lutterotti, L.; Quiros, M.; Serebryanaya, N. R.; Moeck, P.; Downs, R. T.; Le Bail, A. Crystallography Open Database (COD): An Open-Access Collection of Crystal Structures and Platform for World-Wide Collaboration. *Nucleic Acids Res.* **2012**, *40*, D420-D427.

(36) Ito, E.; Yamazaki, D.; Yoshino, T.; Shan, S.; Guo, X.; Tsujimo, N.; Kunimoto, T.; Higo, Y.; Funakoshi, K. High Pressure Study of Transition Metal Monoxides MnO and CoO: Structure and Electrical Resistance. *Phys. Earth Planet. Inter.* **2014**, *228*, 170-175.

(37) Wang, Q.; Li, S.; He, Q.; Zhu, W.; He, D.; Peng, F.; Lei, L.; Zhang, L.; Zhang, Q.; Tan, L. et al., Reciprocating Compression of ZnO Probed by X-Ray Diffraction: The Size Effect on Structural Properties under High Pressure. *Inorg. Chem.* **2018**, *57*, 5380-5388.

(38) Birch, F. Finite Strain Isotherm and Velocities for Single-Crystal and Polycrystalline NaCl at High Pressures and 300°K. *J. Geophys. Res.: Solid Earth* **1978**, *83*, 1257-1268.

(39) Mitra, S. *High-Pressure Geochemistry and Mineral Physics: Basics for Planetology and Geo-Material Science, 1st Edition*; Elsevier: Amsterdam, Boston, 2004.

(40) Klotz, S.; Chervin, J. C.; Munsch, P.; Le Marchand, G. Hydrostatic Limits of 11 Pressure Transmitting Media. *J. Phys. D: Appl. Phys.* **2009**, *42*, 075413.

(41) Fernando, S.; Baynes, M.; Chen, B.; Banfield, J. F.; Zhang, H. Compressibility and Structural Stability of Nanoparticulate Goethite. *RSC Adv.* **2012**, *2*, 6768-6772.

(42) Silberberg, M. *Principles of General Chemistry, 3rd Edition*; McGraw-Hill Education: New York, 2012.

## TOC Graphic